

You-dong MAO, Chun-xiong LUO, Qi OU-YANG

Reversibly switchable DNA nanocompartment on surfaces: experiments, applications, and theory

© Higher Education Press and Springer-Verlag 2008

Abstract This paper summarizes our studies of DNA nanocompartment in recent years. Biological macromolecules have been used to fabricate many nanostructures, bio-devices, and biomimetics because of their physical and chemical properties. But dynamic nanostructure and bio-machinery that depend on collective behavior of biomolecules have not been demonstrated. Here, we report the design of DNA nanocompartment on surfaces that exhibit reversible changes in molecular mechanical properties. Such molecular nanocompartment is served to engage molecules, switched by the collective effect of Watson-Crick base-pairing interactions. This effect is used to investigate the dynamic process of nanocompartment switching and molecular thermosensing, as well as perform molecular recognition. Further, we found that ‘fuel’ strands with single-base variation cannot afford an efficient closing of nanocompartment, which allows highly sensitive label-free DNA array detection. Theoretical analysis and computer simulations confirm our experimental observations, which are discussed in this review paper. Our results suggest that DNA nanocompartment can be used as building blocks for complex biomaterials, because its core functions are independent of substrates and mediators.

Keywords DNA nanocompartment, DNA array, Molecular collective behavior, molecular channel

PACS numbers 87.14.Gg, 87.15.-v, 87.15.He, 87.15.Aa

You-dong MAO, Chun-xiong LUO, Qi OU-YANG (✉)

School of Physics, Key Laboratory for Mesoscopic Physics, and Center for Theoretical Biology, Peking University, Beijing 100871, China
E-mail: qi@pku.edu.cn

Received January 5, 2008; accepted January 10, 2008

1 Introduction

Biological macromolecules with amazing polymorphism have shown their ability in molecular machinery [1–3], devices [4, 5], and computation [6]. In principle, such ability could incorporate the molecular ‘bottom-up’ approach [7–9], leading to a nanostructure with potential for molecular device applications. Building blocks with properties independent of substrates or mediators are undoubtedly significant to developing a functional and complex nanosystem. Mechanical behavior of single or few bio-molecules has been well demonstrated [1–3]. It is difficult, however, to use these molecular machines as the building blocks of a complex nanosystem. The implementation of a bio-molecular mechanical device that depends on the collective behavior of molecules on a surface, which in principle would provide a kind of building blocks with the above-mentioned feature, remains challenging. While a recent study reports the design of a reversibly switching surface [10], the study of dynamic collective behavior is still in its early age. Efforts to engineer a surface switched by bio-molecular mechanical properties may lead new breakthroughs in nanomaterial researches.

Recently, we found that specially designed DNA array can form a molecular cage on surfaces [11–13]. This molecular cage is switchable due to allosteric transformation driven by the collective hybridization of DNA. We named it “active DNA nanocompartment (ADNC)”. Typical DNA motif designed to fabricate ADNC comprises two contiguous elements [inset to Fig. 1(a)]: a double-stranded DNA (dsDNA) whose array is responsible for a compact membrane [Fig. 1(a), *right*], and a single-stranded DNA (ssDNA) serving as skeleton supporting the dsDNA membrane, which is terminated on its 5' end by a surface linker such

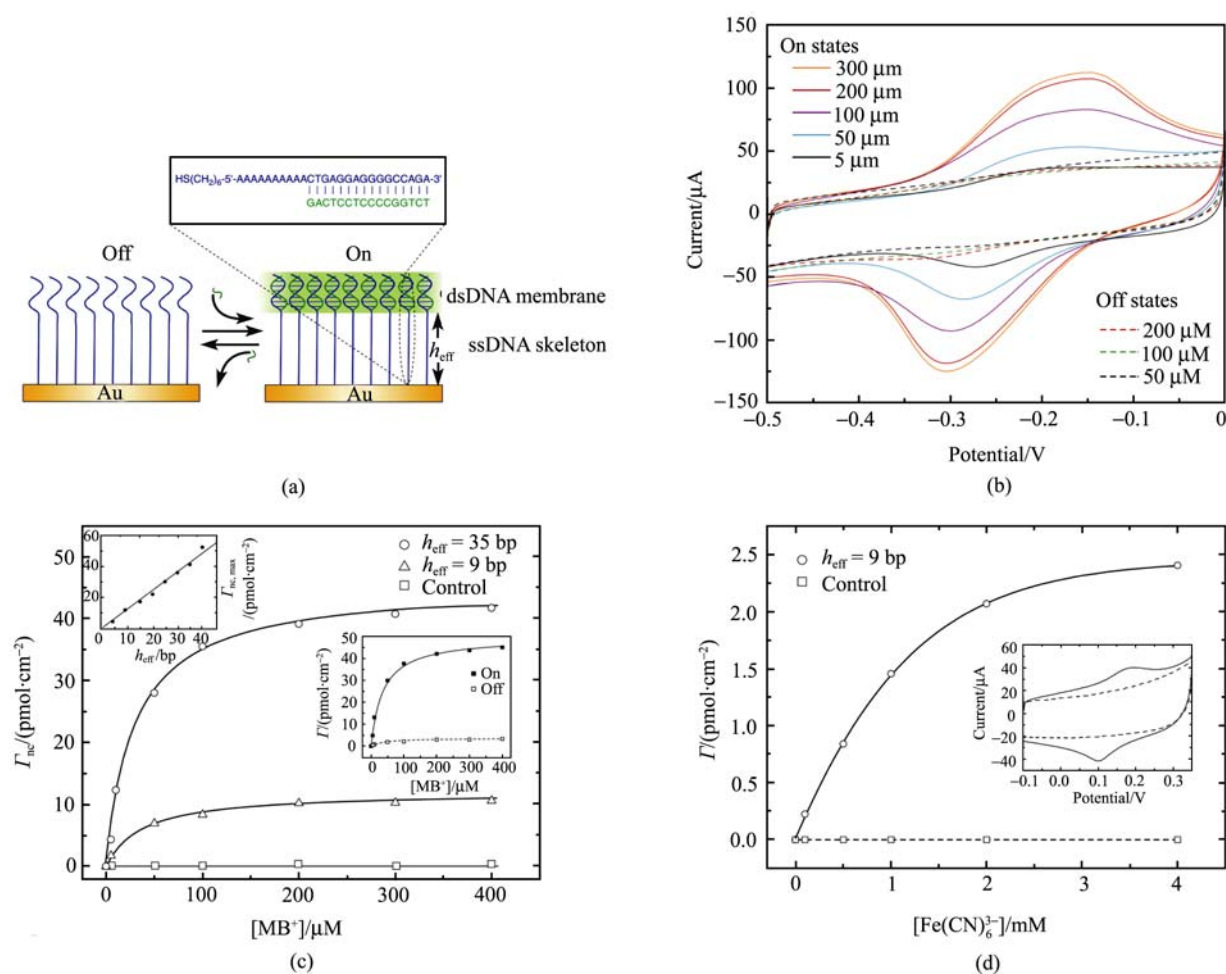


Fig. 1 (a) Schematic drawing of a dual-state ADNC. By adding or removing ‘fuel’ strands (green), the ADNC can be switched between on (right) and off (left) state. Inset, a typical sequence used to fabricate ADNC. The green ‘fuel’ strands is a segment of human p53 gene containing one site of most frequent mutation. (b) Original cyclic voltammograms of ADNC for the on and off states with different $[MB^+]$ configurations. Insets show the $[MB^+]$ corresponding to each colorized curve. Scan rate = 4 V s^{-1} . Sample interval = 0.001 V . (c) Isotherms for MB^+ in an on-state ADNC at room temperature. Γ_{nc} is the difference between Γ measured in the on state and the off state. (Right inset) The relationship of $\Gamma_{nc,max}$ and h_{eff} . The slope of $\Gamma_{nc}-h_{eff}$ curve ($\sim 10 \text{ mM}$) represents the saturation concentration. The on/off ratio of the amount concentration (I) for MB^+ confined ranges from 10 to 18. Control experiments (open square) were based on the samples with a low density of the same DNA motifs ($\sim 1.6 \times 10^{12} \text{ molecules cm}^{-2}$). (d) Isotherms for $[Fe(CN)_6]^{3-}$ in an on-state ADNC at room temperature ($h_{eff} = 9 \text{ bp}$). Inset shows typical cyclic voltammogram on an on-state ADNC encaging $[Fe(CN)_6]^{3-}$ ($[Fe(CN)_6]^{3-} = 2 \text{ mM}$). Scan rate = 1 V s^{-1} . Dashed line shows the control experiments performed on the ADNC that was hybridized with single-base mismatches. The ratio for $[Fe(CN)_6]^{3-}$ almost reaches more than 100.

as an alkanethiol group that can immobilize DNA on gold surface with a sulphur-gold bond [14–19]. Because the diameter of ssDNA is much smaller than that of dsDNA, a compartment with designable effective height (h_{eff} , 5–50 nm, commensurate with the length of ssDNA skeleton) can form between the dsDNA membrane and substrate surface.

In this review article, we discuss some basic properties of ADNC, explore its implication in practical utility, and then give a theoretical explanation of key characteristics of such a device. We will show that ADNC switching is controllable, and dynamic process of ADNC closing is step by step. By

introducing self-assembly monolayer, we further reconstruct it into a surface system that is thermally sensible to special molecules. By tuning the switching temperature, one can control the behavior of the system in molecule release. Furthermore, we find that target sequences with single-base variation cannot afford an efficient closing of ADNC. This study also suggests that the property of ADNC is independent of substrate and indicator.

In the theoretical studies, we report of simulation studies of melting transition on DNA Nanocompartment using Monte Carlo method, this shows the collective behavior of the nanocompartment and explains the high selective of this

DNA chips [20]. We also use stochastic modeling to build a Fork-Planck equation to describe the dynamic behavior of the system [21], the model is quantitatively agrees with the experimental observation on ADNC closing.

2 Experiment

2.1 Rational design in interfacial engineering

A typical DNA motif is shown in inset to Fig. 1(a). The ‘fuel’ strand [green in inset to Fig. 1(a)] used to switch the DNA compartment is selected from the human p53 gene, one of the frequently mutated residues. A conformational transition between ‘on’ and ‘off’ states of ADNC requires synergistic molecular reorganization of ordered DNA motif. In principle, the formation of ADNC depends on three conditions: (1) whether the dsDNA portion can be densely packed into a relatively impermeable membrane; (2) whether the dsDNA membrane can be formed reversibly by *in situ* hybridization; and (3) whether the nanocompartment can continuously span across a sufficient area. Dense molecular packing of ssDNA self-assembled monolayer (SAM) and strong interactions between the sugar-phosphate backbones of ssDNA restrict molecular hybridization [14–19, 22]. However, 100 % hybridization efficiency is achievable if the density is in a proper range (supposing that other factors are fixed) [14, 15, 22]. Theoretical expectation of the optimum density for ADNC formation is $(5 \pm 2) \times 10^{12}$ molecules cm^{-2} ; lower or higher density will notably result in the failure of its formation. To establish sufficient spatial freedom for molecular hybridization, we have ssDNA capped by a helical dsDNA segment [green in Fig. 1(a)] before the ssDNA motif self-assembled on the surface. This results in a SAM that is densely packed with respect to the space-filling helical cap, but shows low-density packing with respect to the ssDNA skeleton. Subsequent removal of the space-filling helical cap by denaturation establishes an appropriate density of ssDNA SAM, which is measured to be $(5.4 \pm 0.8) \times 10^{12}$ molecules cm^{-2} , within the optimum density range. Similar methods to control self-assembly density can be found in other reports [10, 23].

2.2 Experimental definition on the basic structure of ADNC

To experimentally define the basic nanostructure of ADNC, we characterized the surface of the ADNC film using atomic force microscopy (AFM). We investigated the thickness

changes of ADNC with different base numbers of its ssDNA skeleton by measuring the profiles of the ADNC film at its edge. The results presented in Fig. 2(a) show that the thickness of ADNC increases linearly with elongation of the ssDNA skeleton. The slope of the curve is about 0.8 ± 0.2 nm per base. Because the tapping mode of ATM measurement often gives a systematic error in z -direction, the data is

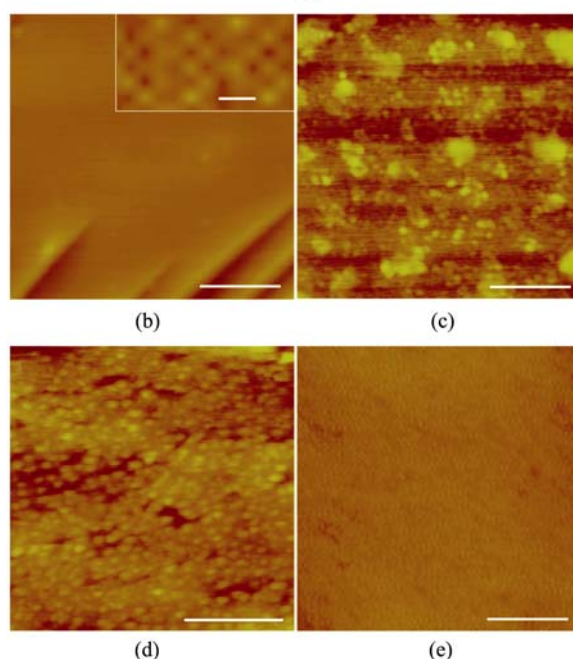
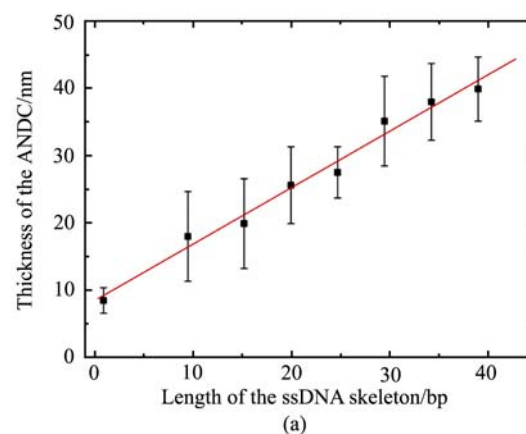


Fig. 2 AFM measurements of ADNC on Au(111) surface. **(a)** The thickness, measured on the edge of the ADNC, as a function of the length of the ssDNA skeleton. **(b)** The initial on state of the ADNC. The inset shows a crystalline lattice with the periodicity of 4.0 ± 0.5 nm, which was found on well-formed dsDNA membrane. The diameter of one dsDNA molecule can be directly measured to be about 2 nm, proving the image is the top view of dsDNA. **(c)** The off state of the ADNC after denaturation, which shows local aggregation of immobilized ssDNA. **(d)** Insufficient rehybridization, which offers a medium inhomogeneous array to the extent between **(b)** and **(d)**. **(e)** The on state of the device after sufficient rehybridization. Height scale 50 nm as in **(b)**, 10 nm as in **(d)**, **(e)**, 5 nm as in the inset to **(b)**. Scale bars are 250 nm in **(b)**–**(e)**, 5 nm in the inset to **(b)**.

slightly larger than the measured object. If we consider the low limit of error bar and the systematic error in measuring, the data is roughly agree with the measurement reported in the documents [24, 25]. This indicates that the immobilized DNA motifs are oriented perpendicular to the gold surface, which is consistent with the results presented in the literatures [15–17].

Figure 2 (b)–(e) shows topographic observations of the same ADNC sample at different conditions. The topographies of the initial ‘on’ state of the freshly prepared device and subsequent ‘off’ state, achieved by denaturation, are shown in Fig. 2(b) and (c), respectively. The image taken after sufficient rehybridization [Fig. 2(c)] provides a reformed homogeneous array of dsDNA [compared with Fig. 2(c), (d)], verifying that the switching of ADNC is reversible. These direct observations agree that high hybridization efficiency (~100 %) was yielded in our experiments [15–19]. Additional tests further confirm the reliability of the sample used in this comparison.

Surface defects, mostly pinholes, inevitably prevent a perfect ADNC from spanning across a very broad area, and thus are prone to damage the ADNC performance. We have electrochemically evaluated the overall effect of the pinholes on the ADNC film. The results, as shown in Fig. 1(b)–(d), demonstrate that the diffusion of redox reporters through the pinholes can be safely neglected on a macroscopic scale. We thus have clarified the three issues raised above and shown a well-defined nanostructure of ADNC.

2.3 Molecular encaging effect

Since ADNC is reversibly switchable, it should be able to encage molecules with suitable size. We name this phenomenon molecular encaging effect. To examine this effect, we used ADNC to encage certain electroactive species. Redox reactions of these species near the gold surface allow us to address it by electrochemical methods [17, 26]. Methylene blue (MB^+), a phenothiazinium dye [27–29], and ferricyanide anions [30] ($[\text{Fe}(\text{CN})_6]^{3-}$) were chosen as redox reporters, for they are impermeable through the dsDNA membrane of the ADNC. The devices were initially set to the ‘off’ state and exposed to a hybridization solution containing both the ‘fuel’ strands and the reporters for at least 2–3 hours. Once the closed ADNC entrapped some reporters, the surface concentration (Γ_{nc}) of the encaged reporters could be determined by cyclic voltammetry [Fig. 1(b)]. Figure 1 (c) and (d) give the isotherms of the molecular encaging effect for MB^+ and $[\text{Fe}(\text{CN})_6]^{3-}$ respectively. Control experiments show that high density of immobilized ssDNA ($> 8 \times 10^{12}$

molecules cm^{-2}) would notably decrease the ‘on/off’ ratio to 1–2, due to the low hybridization efficiency and the failure of ADNC formation, and that low density ($< 2 \times 10^{12}$ molecules cm^{-2}) results in the vanishing of Γ_{nc} . These isotherms all fit well to the Langmuir model [26]: $x/\Gamma_{\text{nc}} = (1/\Gamma_{\text{nc,max}})x + 1/(K\Gamma_{\text{nc,max}})$, where x is the concentration of the reporter and K is the association constant per site [14, 17]. The isotherms at different h_{eff} for MB^+ [Fig. 1(c)] give the same K value, showing that single-site binding mode dominates in interactions between ADNC and reporters. While MB^+ obtained $K = (3.0 \pm 0.2) \times 10^4 \text{ M}^{-1}$, $[\text{Fe}(\text{CN})_6]^{3-}$ obtained $K = (0.9 \pm 0.1) \times 10^3 \text{ M}^{-1}$. The difference demonstrates that the electronegativity of $[\text{Fe}(\text{CN})_6]^{3-}$ prominently diminished the capacity of ADNC.

The linear relationship between the saturation of Γ_{nc} ($\Gamma_{\text{nc,max}}$) and h_{eff} shown in the left inset of Fig. 1(c) demonstrates that the number of encaging sites is proportional to the length of the ssDNA skeleton, providing experimental evidence that the closed ADNC can be considered as a container. The saturation concentration of MB^+ in the closed ADNC is several orders of magnitude higher than $[\text{MB}^+]$ in external solution, but is in the same order of magnitude as the concentration of the negative charges provided by ssDNA skeletons (~50 mM). This suggests that the electrostatic interactions between the negatively charged sugar-phosphate backbone of ssDNA skeleton and the MB^+ cations caused MB^+ to fill up the space of the ADNC. The electrostatic interaction is strongly affected by the ionic strength of the operation solution [14, 31, 32]. We observed that increasing $[\text{Na}^+]$ could decrease Γ_{nc} due to the competition between Na^+ and MB^+ . At $[\text{Na}^+] = 0.5 \text{ M}$, no encaging effect was observed even using high $[\text{MB}^+]$ (0.5 mM). In contrast to MB^+ , the saturation concentration of the encaged $[\text{Fe}(\text{CN})_6]^{3-}$ (~10 mM) is at the same order as the concentration of $[\text{Fe}(\text{CN})_6]^{3-}$ in the external solution. These results suggest that the capacity of ADNC is determined by the interaction between the encaged species and ADNC backbones, and that the molecular encaging effect is a general property of ADNC.

To further verify the generality of ADNC properties, we also constructed ADNC on a SiO_2 substrate and used fluorescein ($\text{C}_{20}\text{H}_{10}\text{Na}_2\text{O}_5$) as optical reporters. Because fluorescein molecules are impermeable through the dsDNA membrane of ADNC, they can be encaged by the ADNC on SiO_2 substrate. Our experimental result by fluorescent microscopy shows similar behavior compared to $[\text{Fe}(\text{CN})_6]^{3-}$ and MB^+ . In addition, some DNA motifs with different base numbers in dsDNA membrane, ranging from 9 to 30, are also used to validate the molecular encaging effect.

2.4 Single-base mismatch detection using ADNC switching

Although we have used perfectly complementary strands as ‘fuel’ molecules to switch ADNC, whether strands with base mismatches could also work remains unclear. To work out this question, we designed a series of experiments to evaluate discrimination of the complementary pair, G:C, from the three single-base mismatches, G:X (X = A, T, G), which is the point mutation site in the human p53 gene.

Typical performance is shown in Fig. 3. Using the engaged species as hybridization indicators greatly sharpens the melting profiles for the perfectly complementary targets, and flattens denaturation profiles for the strands with a wobble

mismatch. This shows that single-base mismatched strands are incapable of closing ADNC. Experiments regarding the dynamic properties of ADNC (Fig. 3) have suggested that hybridization efficiency below a certain value (70 ± 4 %) cannot cause an efficient closing of ADNC, which results in a sharp drop in the melting transition. The flattening of the thermal-denaturation curve for mismatches was, therefore, attributed to the low efficiency of hybridization for mismatches, which was measured to be less than 50 % by quartz crystal microbalance [18]. While the fluorescence-labeling-based system has 2.6:1 selectivity at its optimum stringency temperature (42 °C), ADNC-based system increases this selectivity to about 100:1 at a temperature ranging from 10 °C to 45 °C. The improved selectivity in the assay results from the switching of ADNC that depends on a fully collective hybridization. Since the two kinds of substrates (gold, SiO₂) and three kinds of indicators (MB⁺, [Fe(CN)₆]³⁻, fluorescein C₂₀H₁₀Na₂O₅) used in these investigations show consistent results, we conclude that the molecular recognition property of ADNC between matches and mismatches is independent of substrates and indicators. Different realization and implementation of ADNC, however, would reasonably result in a different selectivity and sensitivity. These results suggest that ADNC provides a novel approach to sequence-specific recognition of DNA.

In the section of theoretical analysis, we will use Monte Carlo simulation to show that the collective behavior of the dsDNA film is responsible for the high selectivity of the ADNC.

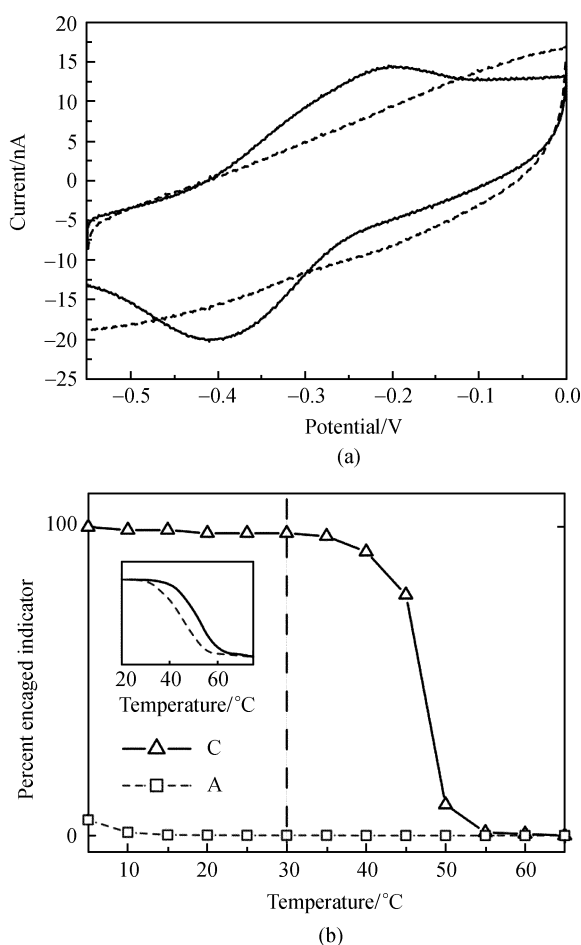


Fig. 3 (a) Typical cyclic voltammograms of an ADNC system with 10 μm diameter for the wild type target (solid line) and the single mismatch (dashed line) measured at 25 °C, using the engaged molecule as hybridization indicator. (b) Dissociation of target from the surface of this ADNC system. Black curves describe DNA duplex thermal-denaturation curve for the perfectly complementary oligonucleotide (X = C), and gray dashed curves for the strand with a wobble mismatch (X = A). The intercepts at the vertical dotted line allow one to estimate the expected ratio of engaged indicator at complementary and mismatched array elements. (Inset) Thermal-denaturation curve monitored by fluorescence-labeling for the perfectly matched DNA (X = C) and the one with a wobble mismatch (X = A).

2.5 Dynamic process on the switching of ADNC

The isotherms of the molecular engaging effect describe well the static behavior of a closed ADNC, however, the dynamic process of its switching needs a further investigation. To investigate the dynamic feature of ADNC, we introduced phenylenediisothiocyanate (PDC) SAM on the bottom of the nanocompartment [Fig. 4(a)]. In this system, thionine (TH⁺) was used as sensing reporter [33], while PDC was found to be a TH⁺ receptor. We measured the surface concentration (Γ) of TH⁺ as a function of temperature after the system stored TH⁺. The Γ - T curves of the ‘off’ state and the pure PDC SAM (control) both fit to exponential decay [Fig. 4(b)], indicating that the receptors release sensing reporters with increasing temperature and vice versa. The different responses of Γ to abrupt change in temperature [inset to Fig. 4(b)] at the two states give evidence that the closed ADNC prevents the sensing reporters from diffusing across the dsDNA membrane, therefore stabilizing the chemical equilibrium on the receptor layer and storing electrochemical energy.

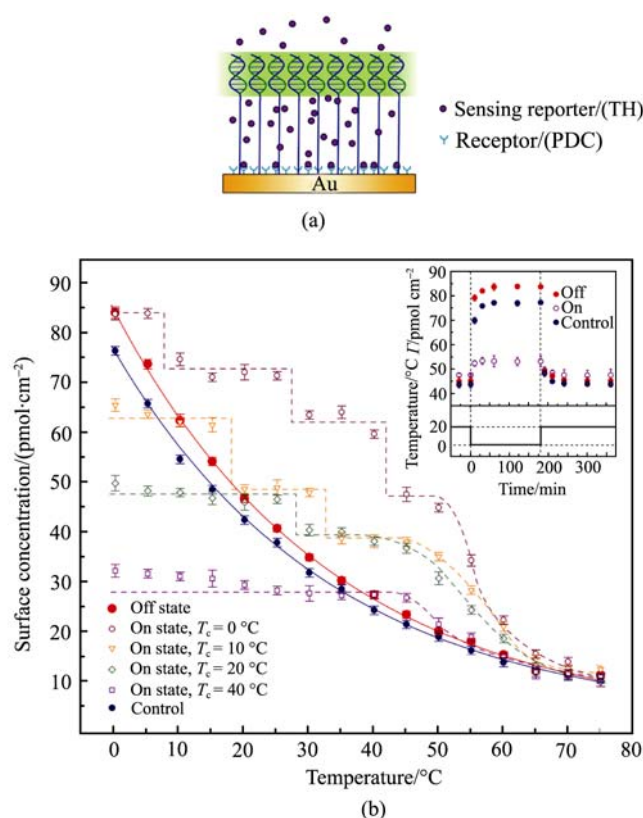


Fig. 4 (a) Schematic drawing of a typical surface system derived from ADNC ($h_{\text{eff}} = 9$ bp). (b) Thermosensing properties of the surface system. The solid lines for the off state (red) and control (blue) are fitted by exponential decay. Γ - T curves of the on state of the ADNC closed at different T_c give different thermosensing modes of the nanosystem. The Γ - T profiles of the on state are plotted by increasing the temperature from 0 °C to 75 °C (positive scan). One observes that the values of Γ at T_c in the Γ - T profiles of the on state are the same as those of the off state (red line). And T_c is always located in the highest step. In addition, the negative scan of the on state from 75 °C to 0 °C (not shown) is always like the positive scan with $T_c = 40$ °C (square). (Inset) abrupt change of temperature triggers the receptor layer to release or store the sensing reporters. The on state corresponds to $T_c = 20$ °C.

To test more effects, we first turned on the ADNC at a certain hybridization temperature (T_c), and then profiled the Γ - T curves by the scan from 0 to 75 °C. Figure 4(b) summarizes the Γ - T curves of the same ADNC that was turned on at the indicated T_c . A notable feature is that multiple steps appear in these Γ - T profiles below the melting point of dsDNA (48 °C). This phenomenon can be explained as follows: The increase in temperature causes the receptors to release sensing reporters and thereby enhances the reporter's concentration in the nanocompartment. When osmotic pressure difference due to sensing reporters surpasses a certain threshold, the dsDNA membrane is temporally broken, thereby allowing sensing reporters to flow between the nanocompartment and external solution, resulting in the transition from one step to the next in Γ - T curves. The steady surface concentration (flat portion of the step) is indicative of molecules that

have been released from their receptors, but have not been allowed to leave the compartment because of the encaging effect. Because T_c can control the initial number of receptors bound with sensing reporters, the events of dsDNA membrane breakage at different temperature and the number of steps in these Γ - T profiles is a function of T_c . Consequently, T_c control provides an approach to modulate the thermosensing mode and molecular release of the surface system. In the next section, we will provide a quantitative analysis on this effect.

3 Theoretical analysis

3.1 Thermodynamic analysis of DNA denaturation of ADNC

Studies on the physical chemistry of DNA denaturation have been lasted for almost forty years [34–36]. In 1964, Lifson proposed that a phase transition exists in one-dimensional polymer structure. He introduced several pivotal concepts, like sequence partition function, sequence generating function, etc., and established a systematic method to calculate the partition function [34]. These allow us to derive important thermodynamic quantities of the system. In 1966, Poland and Scheraga applied Lifson's method to conduct research on amino acid and nucleic acid chains. They built Poland-Scheraga (PS) model for calculating the sequence partition function and discussing the behavior of polymers in melting transitions.

Another excellent progress would be the building of Peyrard-Bishop (PB) model [37, 38] for DNA chains. In PB model, the Hamiltonian of a single DNA chain, which is constructed by phonon calculations, is given so that we can obtain the system properties through statistical physics method. The PB model has introduced mathematical formula of stacking energy, as well as the kinetic energy and potential energy of each base pair. By theoretical calculation, one can show the entropy-driven transition that leads DNA to shift from ordered state to disorder one [39, 40].

However, all these works have not involved the DNA-DNA interactions because the subject investigated is DNAs in bulk solution, and the interaction between them has ever been neglected. The main idea of this part of work is to inspect the influence of collective effect on the DNA melting process, motivated by the experiment results of DNA nanocompartment presented above [11–14]. Under the enlightenment of Poland-Scheraga model and Zimm-Bragg model [41], we simplified Peyrard-Bishop model to meet a reasonable Monte Carlo simulation by the elucidation of five

components of energy changes during melting transition. The result shows that the DNA-DNA interactions in the ADNC are account for the high selectivity of the device.

Taking into account the directional specificity of the hydrogen bonds, the Hamiltonian of a single DNA chain is obtained as following form according to PB model [37–39]:

$$H_y = \sum_n \left[\frac{1}{2} m y_n^2 + w(y_n, y_{n-1}) + V(y_n) \right] \quad (1)$$

where the y_n is the component of the relative displacement of bases along the direction of hydrogen bond. The stacking energy $w(y_n, y_{n-1})$ corresponds to the interaction between neighboring base pair in one DNA chain:

$$w(y_n, y_{n-1}) = \frac{k}{2} [1 + \rho e^{-\alpha(y_n + y_{n-1})}] (y_n - y_{n-1})^2 \quad (2)$$

The Morse potential $V(y_n)$ describes the potential for the hydrogen bonds:

$$V(y) = D(e^{-ay} - 1)^2 \quad (3)$$

However, in this study, the Hamiltonian in Eq. (1) is not sufficient; it neglects the structure of close-packing of DNA in ADNC. In our system, one should take into account the interactions between the nearest neighboring molecules [42, 43]. To model the interaction, one envisions the molecules as rigid cylinders, carrying helical and continuous line charges on their surfaces. Each DNA duplex carries the negative charge of phosphates plus a compensating positive charge from the adsorbed counterions. Let $0 < \theta < 1$ be the degree of charge compensation, f_1, f_2 and f_3 the fractions of condensed counterions in the minor and major grooves ($f_1 + f_2 + f_3 = 1$). The mobile counterions in solution screen the Coulomb interactions between the two molecules, causing at large separations an exponential decay of the latter with the Debye screening length κ^{-1} . The solvent is accounted for by its dielectric constant ϵ . The structural parameters of B-DNA are half azimuthal width of the minor groove $\tilde{\phi}_s \approx 0.4\pi$, pitch $H \approx 34 \text{ \AA}$ ($g = 2\pi/H$), and hard-core radius $a = 9 \text{ \AA}$. We take the following form for the pair interaction potential [44–47]:

$$u(R, \phi) = u_0 \sum_{n=-\infty}^{\infty} [f_1 \theta + (-1)^n f_2 \theta - (1 - f_3 \theta) \cos(n\tilde{\phi}_s)]^2 \frac{(-1)^n \cos(ng\Delta z) K_0(\kappa_n R) - \Omega_{n,n}(\kappa_n R, \kappa_n a)}{(\kappa_n / \kappa)^2 [K'_n(\kappa_n a)]^2} \quad (4)$$

where $R (> 2a)$ is the distance between the two parallel DNA molecules, Δz a vertical displacement, equivalent to a “spin

angle” $\phi = g\Delta z$. Here, $u_0 = 8\pi\sigma^2/\epsilon\kappa^2$ (about $2.9k_B T/\text{\AA}$ at physiological ionic strength), and $\kappa_n = \sqrt{\kappa^2 + n^2 g^2}$. $\Omega_{n,m}(x, y)$ is given by

$$\Omega_{n,m}(x, y) = \sum_{j=-\infty}^{\infty} \left[K_{n-j}(x) K_{j-m}(y) \frac{I'_j(y)}{K'_j(y)} \right]$$

with the modified Bessel functions $K_n(x)$ and $I_j(y)$. The primes denote derivatives. The sum rapidly converges, and it can be truncated after $|n| = 2$. Since $\kappa_n R > 3$ and $g \sim \kappa$, each of the terms in the sum decreases exponentially at increasing R with the decay length $\kappa_n^{-1} \propto 1/n$.

Figure 5 present a scheme of interaction between two neighboring columnar DNA molecules charged with counterions on its surface. The distance between two DNA columns in our simulation is about 30 \AA and the helical pitch of DNA molecule is about 36 \AA . For brevity, we take the mean-field approximation that the pair interactions mainly exist between charges in the same height.

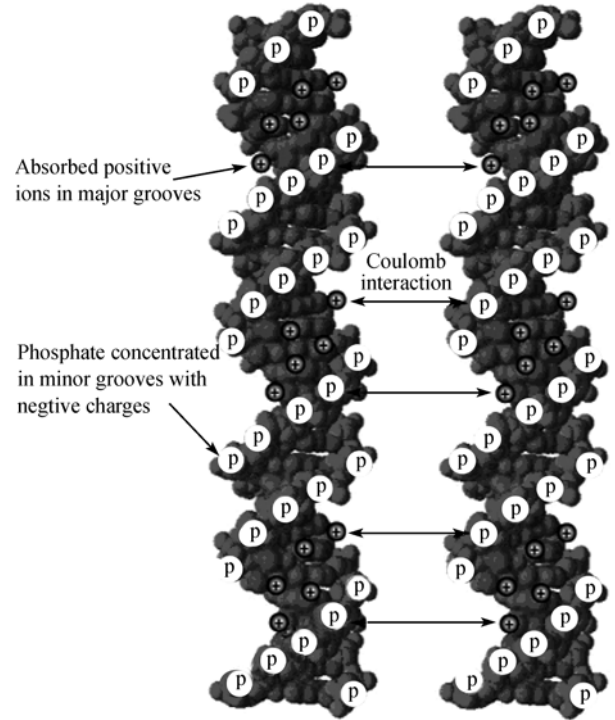


Fig. 5 The pair interaction between two parallel B-DNA double helices. The black balls with positive signs in the center represent the adsorbed positive counterions, while the little grey balls represent the phosphate carrying negative charges. Each DNA duplex carries the negative charge of phosphates with area density of $16.8 \mu\text{C}/\text{cm}^2$ plus a compensating positive charge coming from the adsorbed counterions. We take the assumption that, and the distance between them are approximately 30 \AA .

Now we formulate the Monte Carlo simulation. Let t be the dimensionless variable to mark the time series of simula-

tion ($t = 0, 1, 2, \dots$) and T the environmental temperature. Assuming that $M \times N$ DNAs are on the ADNC, the position of each DNA can be represented by its coordinates (x, y) , where $x, y \in N$, and $0 < x \leq M, 0 < y \leq N$. All DNA molecules in ADNC have identical sequence with P base pairs. Therefore there is the collection of $M \times N \times P$ base pairs. The degree of freedom of the system is also $M \times N \times P$. The position of each base pair is thus represented by coordinates (x, y, i) , where $i \in N, 0 < i \leq P$. We take that the indices of base pairs is assigned from the bottom to the top of the DNA.

At the time t_0 , the state for an arbitrary base pair at (x_0, y_0, i) with well-formed hydrogen bonds is represented as $\psi(x_0, y_0, i, t_0) = 1$. Contrarily, the state of a base pair with decoupled hydrogen bonds is denoted as $\psi(x_0, y_0, i, t_0) = 0$ [39, 48]. $\psi(x, y, i, t)$ is a function of the time and the position of the base pair. Therefore, the state of each DNA molecules in ADNC can be represented by a sequence of digits. The number of all possible states is $2^{M \times N \times P}$.

The simulation begins at $t = 0, T = 0^\circ\text{C}$. At each step, t increases by 1, and state of base pair at (x_0, y_0, i) is inverted, i.e., $\psi(x_0, y_0, i, t+1) = 1 - \psi(x_0, y_0, i, t)$. We assume that by changing the state of the system for $M \times N \times P \times Z$ times, the system will approximate the equilibrium state infinitely. The change will be applied to each base pair for average Z times. Z is determined by experience and should be reasonable. We increase T by ΔT during the simulation. Therefore we have the relation $T = \frac{t}{M \times N \times P \times Z} \Delta T$. Whether the state inversion is permitted depends on the energy change (ΔE_t) in each step. The possibility of the state change at each step is

$$P(\psi(t) \rightarrow \psi(t+1)) = \begin{cases} 1 & \text{for } \Delta E_t < 0 \\ e^{-\Delta E_t / k_B T} & \text{for } \Delta E_t > 0 \end{cases} \quad (5)$$

If the current state change is permitted, we keep up changing the system state at $t+1$. If the state change is forbidden by the possibility, the system state remains unchanged at t and waits for another change at $t+1$.

To achieve a relatively precise simulation, the change of the total energy at time $t+1$ relative to that at the time t is analyzed by five components. The recursion relation of energy change in each step is written as:

$$\Delta E_t = E(t+1) - E(t) = \sum_{l=1}^5 \Delta E_l \quad (6)$$

where $E(t+1)$ and $E(t)$ are the system energy for the instant $t+1$ and t respectively, and $\Delta E_l (l = 1, 2, 3, 4, 5)$ is the varia-

tion of the l th component.

The energy change depends on both the recursion relation of the base pair at (x_0, y_0, i) and the states of its nearest neighbors. The global energy variation is determined by the local states around the base pair (x_0, y_0, i) . Following analysis presents the recursion relation of energy changes.

(1) The hydrogen-binding energy (ΔE_1)

This component of the energy consists of the Morse potential [Eq. (3)] and kinetic energy along the orientation of the hydrogen bonds. The binding energy is independent of the states of its neighboring base pairs,

$$\Delta E_1 = \begin{cases} J & \text{if } \psi(x_0, y_0, i, t) = 0 \\ -J & \text{if } \psi(x_0, y_0, i, t) = 1 \end{cases} \quad (7)$$

where $J (J < 0)$ is the binding energy for each base pair that is in '1' state, while the binding energy for the '0' state is zero to be reference.

(2) The stacking energy (ΔE_2)

To simplify the calculation of the stacking energy shown in Eq. (2), we take into account the states of base pairs at $(x_0, y_0, i-1, t)$ and $(x_0, y_0, i+1, t)$. Their states remain unchanged during the interval from t to $t+1$. We employ the periodic boundary condition (PBC) listed below:

$$\begin{aligned} \psi(x+M, y, i, t) &= \psi(x, y, i, t) \\ \psi(x, y+N, i, t) &= \psi(x, y, i, t) \\ \psi(x, y, i+P, t) &= \psi(x, y, i, t) \end{aligned} \quad (8)$$

Therefore $\psi(x_0, y_0, i-1, t)$ and $\psi(x_0, y_0, i+1, t)$ are both well defined. The stacking energy reflects the interaction between nearest neighboring base pairs in same DNA, and it exists only when two nearest neighbors are in '1' state at the same time. We use the symbol $\psi(x, y, \{i_1, i_2, \dots, i_n\}, t) = \{b_1, b_2, \dots, b_n\}$ to denote states in the same DNA for convenience, which means $\psi(x, y, i_1, t) = b_1, \psi(x, y, i_2, t) = b_2, \dots, \psi(x, y, i_n, t) = b_n$.

$$\Delta E_2 = \begin{cases} 0 & \text{if } \psi(x_0, y_0, \{i-1, i, i+1\}, t) = \{000\} \\ 0 & \text{if } \psi(x_0, y_0, \{i-1, i, i+1\}, t) = \{010\} \\ w & \text{if } \psi(x_0, y_0, \{i-1, i, i+1\}, t) = \{001\} \\ -w & \text{if } \psi(x_0, y_0, \{i-1, i, i+1\}, t) = \{011\} \\ w & \text{if } \psi(x_0, y_0, \{i-1, i, i+1\}, t) = \{100\} \\ -w & \text{if } \psi(x_0, y_0, \{i-1, i, i+1\}, t) = \{110\} \\ 2w & \text{if } \psi(x_0, y_0, \{i-1, i, i+1\}, t) = \{101\} \\ -2w & \text{if } \psi(x_0, y_0, \{i-1, i, i+1\}, t) = \{111\} \end{cases} \quad (9)$$

where w is the stacking energy stored in two nearest neighboring base pairs in '1' state.

(3) Morse potential away from equilibrium point (ΔE_3)

We set $\Delta E_1 = 0$ for the uncoupled hydrogen bond at base

pairs. However, for a '0' state is next near to a '1' state in the same DNA strand, the distance between two base pairs is so close that the Morse potential should be taken into account. We assigned energy E to every two nearest neighboring base pairs that are in different states in the same DNA.

$$\Delta E_3 = \begin{cases} 2E & \text{if } \psi(x_0, y_0, \{i-1, i, i+1\}, t) = \{000\} \\ -2E & \text{if } \psi(x_0, y_0, \{i-1, i, i+1\}, t) = \{010\} \\ 0 & \text{if } \psi(x_0, y_0, \{i-1, i, i+1\}, t) = \{001\} \\ 0 & \text{if } \psi(x_0, y_0, \{i-1, i, i+1\}, t) = \{011\} \\ 0 & \text{if } \psi(x_0, y_0, \{i-1, i, i+1\}, t) = \{100\} \\ 0 & \text{if } \psi(x_0, y_0, \{i-1, i, i+1\}, t) = \{110\} \\ -2E & \text{if } \psi(x_0, y_0, \{i-1, i, i+1\}, t) = \{101\} \\ 2E & \text{if } \psi(x_0, y_0, \{i-1, i, i+1\}, t) = \{111\} \end{cases} \quad (10)$$

(4) The effect of excluded volume (ΔE_4)

The effect of excluded volume in the nature of DNA phase transition is discussed in Fisher's work [20]. The excluded volume effect is connected to the system entropy variation. The effect is prone to separate two complementary strands in a double helix. We use F to represent the energy change corresponding to this effect. One should notice $\partial F/\partial T < 0$. We then have

$$\Delta E_4 = \begin{cases} -F & \text{if } \psi(x_0, y_0, \{i-1, i, i+1\}, t) = \{000\} \\ F & \text{if } \psi(x_0, y_0, \{i-1, i, i+1\}, t) = \{010\} \\ -F & \text{if } \psi(x_0, y_0, \{i-1, i, i+1\}, t) = \{001\} \\ F & \text{if } \psi(x_0, y_0, \{i-1, i, i+1\}, t) = \{011\} \\ -F & \text{if } \psi(x_0, y_0, \{i-1, i, i+1\}, t) = \{100\} \\ F & \text{if } \psi(x_0, y_0, \{i-1, i, i+1\}, t) = \{110\} \\ -F & \text{if } \psi(x_0, y_0, \{i-1, i, i+1\}, t) = \{101\} \\ F & \text{if } \psi(x_0, y_0, \{i-1, i, i+1\}, t) = \{111\} \end{cases} \quad (11)$$

The energy changes discussed above are summarized in the Fig. 6 below, which does not take into account the DNA-DNA interactions so far.

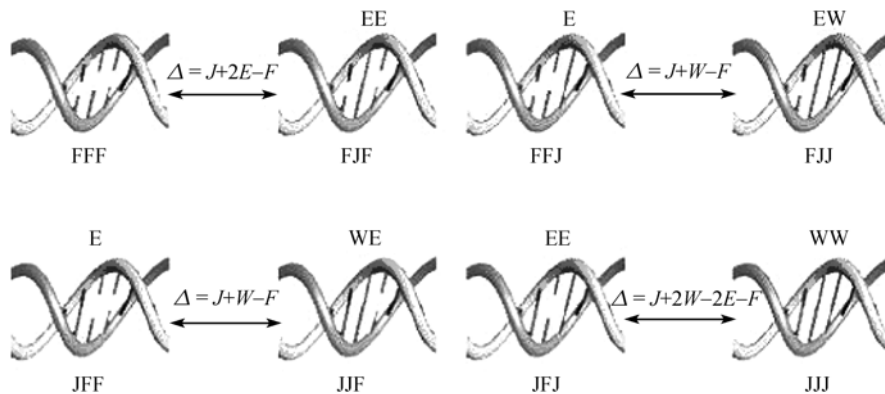


Fig. 6 Scheme for the energy changes. The energy change under every case is formulated when the state of a base pair takes inversion. The value overhanging the double-arrow represents the energy variation when the state changes from left to right. $\Delta = \Delta E_1 + \Delta E_2 + \Delta E_3 + \Delta E_4$.

(5) DNA-DNA interaction potential (ΔE_5)

We have introduced DNA-DNA interaction in previous section. For each base pair, we denote the state of its m nearest neighbors with λ_i ($i = 1, 2, \dots, m; \lambda_i = 0, 1$). ΔE_5 can be written as

$$\Delta E_5 = \begin{cases} G \sum_{i=1}^m \lambda_i & \text{if } \psi(x_0, y_0, i, t) = 0 \\ -G \sum_{i=1}^m \lambda_i & \text{if } \psi(x_0, y_0, i, t) = 1 \end{cases} \quad (12)$$

where G is the interaction energy between each pair of ions. Adding ΔE_5 to Δ , we will get the energy variation including the DNA-DNA interaction.

Following Eqs. (5)–(12), we could achieve a coarse-gained simulation of the melting curves of ADNC as well as that of DNA in bulk solutions. To perform the task, we choose suitable scale parameters to carry out the simulation: $M = 100$, $N = 100$, $P = 20$. The values of M and N chosen are much smaller than ones of the actual situation, which is up to 10^4 in the experiment. Since we take the periodic boundary condition, the values of M and N used do not change our result. The starting temperature is 0°C , and the final temperature is 100°C , with increment of 0.01°C for each step. To guarantee the system reaches equilibrium state, we take 10^6 state changes under a specific temperature. Each base pair has average 5 times to be changed. At each step, we count the number of DNAs that is still hybridized and calculate the percentage for dsDNA in ADNC. The simulation result shown in Fig. 7 shows a steep melting transition (*hollow circles*), consistent to the experimental observations. The simulated result without considering DNA-DNA interaction show in filled circles in Fig. 7 also agrees with the DNA melting curves in bulk solution. Comparison between the two cases suggests that the DNA-DNA interaction greatly increases the melting point of dsDNA chains.

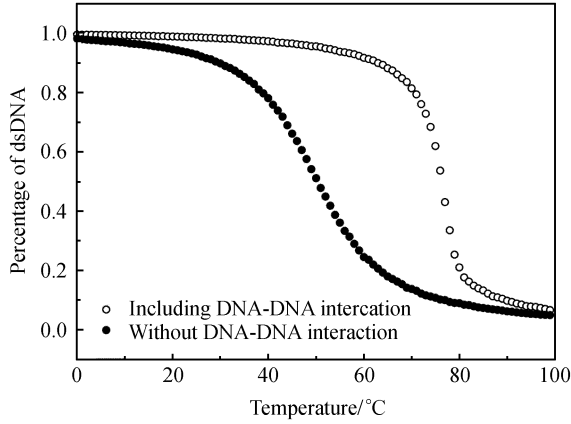


Fig. 7 Simulation results of melting curves for collective DNA molecules. The filled circle represents the phase transition curve without considering the DNA-DNA interaction, while the hollow circle is the counterpart that takes into account the interaction. Parameters used in the simulations are: $J = -1900k_B$, $w = -250 k_B$, $E = 850k_B$, $0.086 eV$, $F = -1650 k_B$, $\partial F / \partial T = -10 k_B$, $G = -125 k_B$.

3.2 Dynamic analysis of ADNC closing

Now we discuss our theoretical analysis on the dynamic behavior of ADNC gating, as presented in the experimental result in Fig. 4. To quantitatively explain our experimental observations, we establish a simple theoretical model based on stochastic dynamics. The gating of DNA channels is described as a diffusion-limited process [49–51]. Two major factors are considered in the equation: a stress $F(t)$ arising from permeating TH molecules and acting on the inner surface of the channel, and an energy landscape of the channel describing the deformation potential during channel's gating. According to our estimation, the time scale of the channel's gating is much larger than that of TH's transport. The screened long-range electrostatic interaction between dsDNA molecules [52, 53] entails high flexibility [54] of the DNA channels, so that the energy landscape of the DNA channels can be described in terms of the channel's radius (R) as an upward parabola shown in Fig. 8(a). Based on this energy landscape, we find the equation governing the channel's motion:

$$\frac{\partial \langle x(t) \rangle}{\partial t} = -\beta D (2\pi\alpha \langle x(t) \rangle - F(t)) \quad (13)$$

where $\langle x(t) \rangle$ is the mean of $x(t) = R(t) - R_0$ over thousands of individual motion trajectories; R_0 is the radius of a free channel of ground energy in equilibrium; D is the conformational diffusion coefficient; α is the area tension on the circumference of the channel; and $\beta = 1/(k_B T)$. Considering the single-file nature of TH permeation through the DNA chan-

nels, our simulation with a one-dimensional lattice model [55] establishes a relationship between $F(t)$ and $C(t)$ [see Fig. 8(b)]:

$$F(t) \approx \frac{pn_m C(t)}{C(t) + \kappa^{-1}} \quad (14)$$

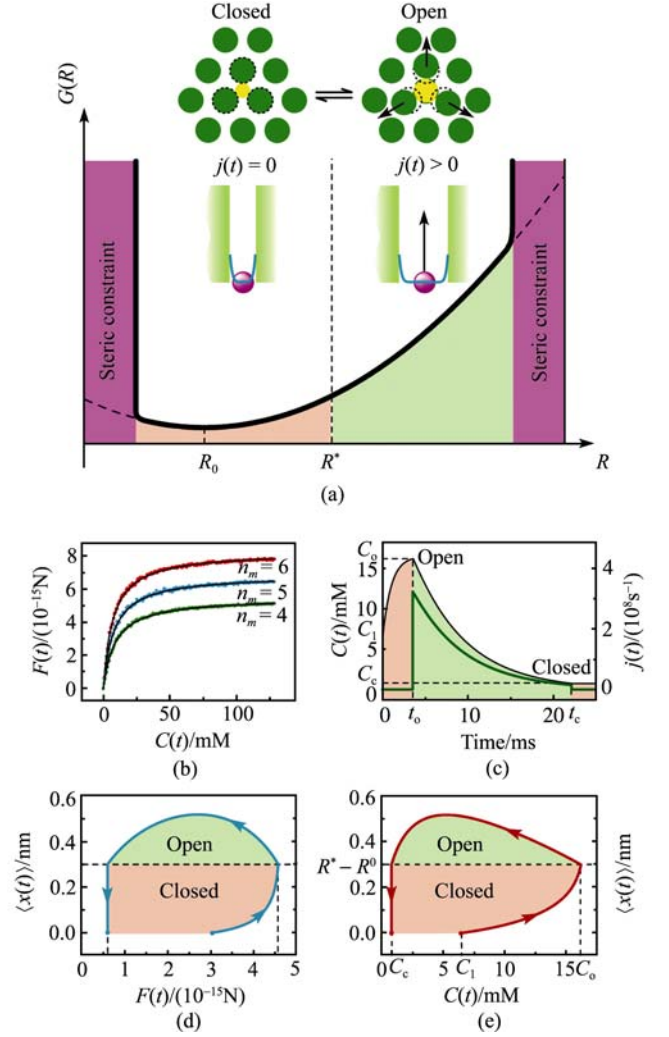


Fig. 8 Theoretical modeling on gating dynamics of DNA channels. (a) The energy landscape of a DNA channel (solid line), with minimum located at abscissa of R_0 . The two regions, corresponding to the closed and open states of the channel respectively, are separated by dashed line at abscissa of R^* . (Upper inset) Top view of the closed (left) and open (right) DNA. (Lower inset) Lateral view of closed (left) and open (right) DNA channels. Purple spheres represent TH; blue lines represent steep-wall potential between TH and DNA channel; and arrow shows the direction of TH transport flux. (b) The simulated mean stress of TH molecules exerting on the inner surface of the DNA channels as a function of TH concentration inside the ADNCs. Black lines fit Eq. (14). Three different lengths of DNA channels are shown, which are $8r$, $10r$, and $12r$ from bottom to top respectively, where r is the radius of TH. (c) A complete cycle of TH pumping coupled with single channel gating. Black and green lines show respectively the time evolution of $C(t)$ and that of $j(t)$. (d) The mean trajectory of $\langle x(t) \rangle$ as a function of $F(t)$. (e) The mean trajectory of $\langle x(t) \rangle$ as a function of $C(t)$.

where p is the mean stress of single TH acting on the inner surface of the channel; n_m is the maximum of the mean residence number of permeating TH inside the channel; and κ is the association constant. This equation reflects the spontaneous change of channel-particle interactions in response to transport flux.

Since the static channel-particle interactions can be simulated by a steep-wall potential [56], there exists a critical radius R^* such that: if $R(t) < R^*$, the channel-particle interactions provide sufficiently large frictions to inhibit the TH to move along the channel, resulting in transport flux $j(t) = 0$. If $R(t) > R^*$, the channel-particle interactions only provide a small viscous friction, γ , allowing the TH to permeate with $j(t) > 0$. Because $j(t)$ is approximately a linear function of $C(t)$ at steady states [57–59], $C(t)$ can be analytically solved. With this information one may numerically resolve the motion trajectories of the DNA channels corresponding to our real experiments.

Figure 8 (c) depicts our numerical result of one complete cycle of TH's pumping through single channel against the nanomechanical deformation potential of the DNA channel. The simultaneous motion trajectories of $\langle x(t) \rangle$ coupled to $F(t)$ and $C(t)$ are depicted in Fig. 8(d) and (e), respectively. The hysteretic trajectory maps the critical radius at $\langle x(t) \rangle = R^* - R_0$ to dual criticality of concentrations [Fig. 8(e)]. Namely, C_o corresponds to the opening criticality of the channel during the increase of $C(t)$, and C_c corresponds to the closing criticality of the channel during the decrease of $C(t)$. Most importantly, $h(C_o - C_c)$ measures the net quantity of TH permeating through the channel during such a pumping, where h is the effective height of the ADNC.

To facilitate the simulation of I - T profiling, we notice that Eqs. (13) and (14) give a threshold concentration:

$$C^* = \kappa^{-1} \{ p n_m / [2\pi\alpha(R^* - R_0)] - 1 \}^{-1} \quad (3)$$

which provides a criterion of channel gating: the channels can be opened only if C_{\max} is larger than C^* , where C_{\max} is the maximum value of $C(t)$ after the increase of temperature triggers the TH's release from PDC SAM. The criterion is well verified by our numerical simulations (data not shown). Figure 9 summarizes the relations between C^* and C_{\max} during the I - T profiling, suggesting five possible cases. The blue line in Fig. 9 demonstrates the case of $C^* > C_{\max}$ within the temperature range of interest, which gives rise to the first type behaviour of I - T profiles. The green line demonstrates the case of $C^* < C_{\max}$ within the temperature range of interest, which gives rise to the second type behavior of I - T profiles. The solid red line demonstrates the case of the mixed type with one crossover at T^* between C^* and C_{\max} , with $C^* > C_{\max}$ at $T < T^*$, making corresponding I - T profiles to hold

the first type behaviour at $T < T^*$ and the second type behaviour at $T > T^*$. The dashed red line demonstrates another case of one crossover between C^* and C_{\max} , with $C^* < C_{\max}$ at $T < T^*$, which gives reverse sequence of the first and second type behaviours in corresponding I - T profiles. The orange line demonstrates the case of the mixture type with two crossover at T_1^* and T_2^* ($T_1^* < T_2^*$), making corresponding I - T profiles to hold the first type behaviour in the range of $T_1^* < T < T_2^*$ and the second type behaviour in the range of $T < T_1^*$ and $T > T_2^*$. Assuming that dsDNA density is homogeneous on surfaces, so that statistically all DNA channels among the dsDNA membrane are faced with the same condition. Given that the distance between opened channel is far apart, the interaction among the opened channels can be omitted. Based on this picture, the above analysis about single channel's gating can be readily extended to simulate the experiments. The same condition will give the same performance, resulting in a concert behavior.

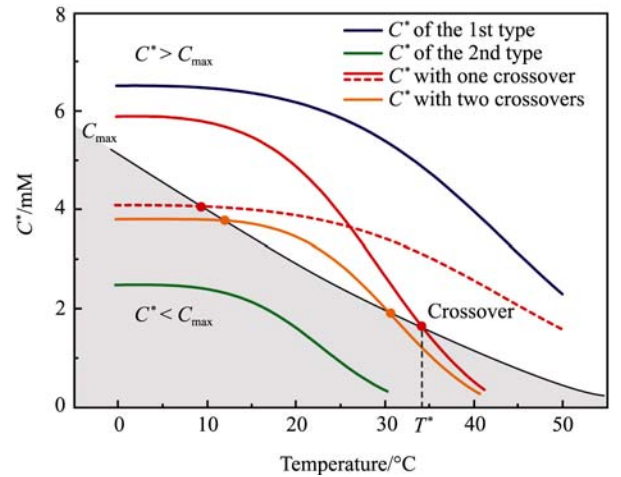


Fig. 9 Behaviour of the gating threshold C^* as compared with C_{\max} . The solid black line sketches the maximum concentration C_{\max} of TH in a closed ADNC with all DNA channels closed. Grey area marks the regime of $C^* < C_{\max}$.

Figure 10 shows quantitative comparisons between simulations and experiments on a variety of typical I - T profiles. Data shown in the figure are all obtained simultaneously from the same run of the simulation using the same parameter set. It suggests that the behaviors of I - T profiles may be classified into two major types. The first type corresponds to $C^* > C_{\max}$ in the temperature range of interest (*blue line* of Fig. 8). Since the release of TH from PDC SAM in 5 °C temperature change is not always enough to increase $C(t)$ to overwhelm C^* , the channels cannot be opened in every measurement step of the I - T profiles, resulting in the step-wise effect [Fig. 10(a)]. The second type corresponds to $C^* < C_{\max}$ in the temperature range of interest (*green line* of Fig. 9).

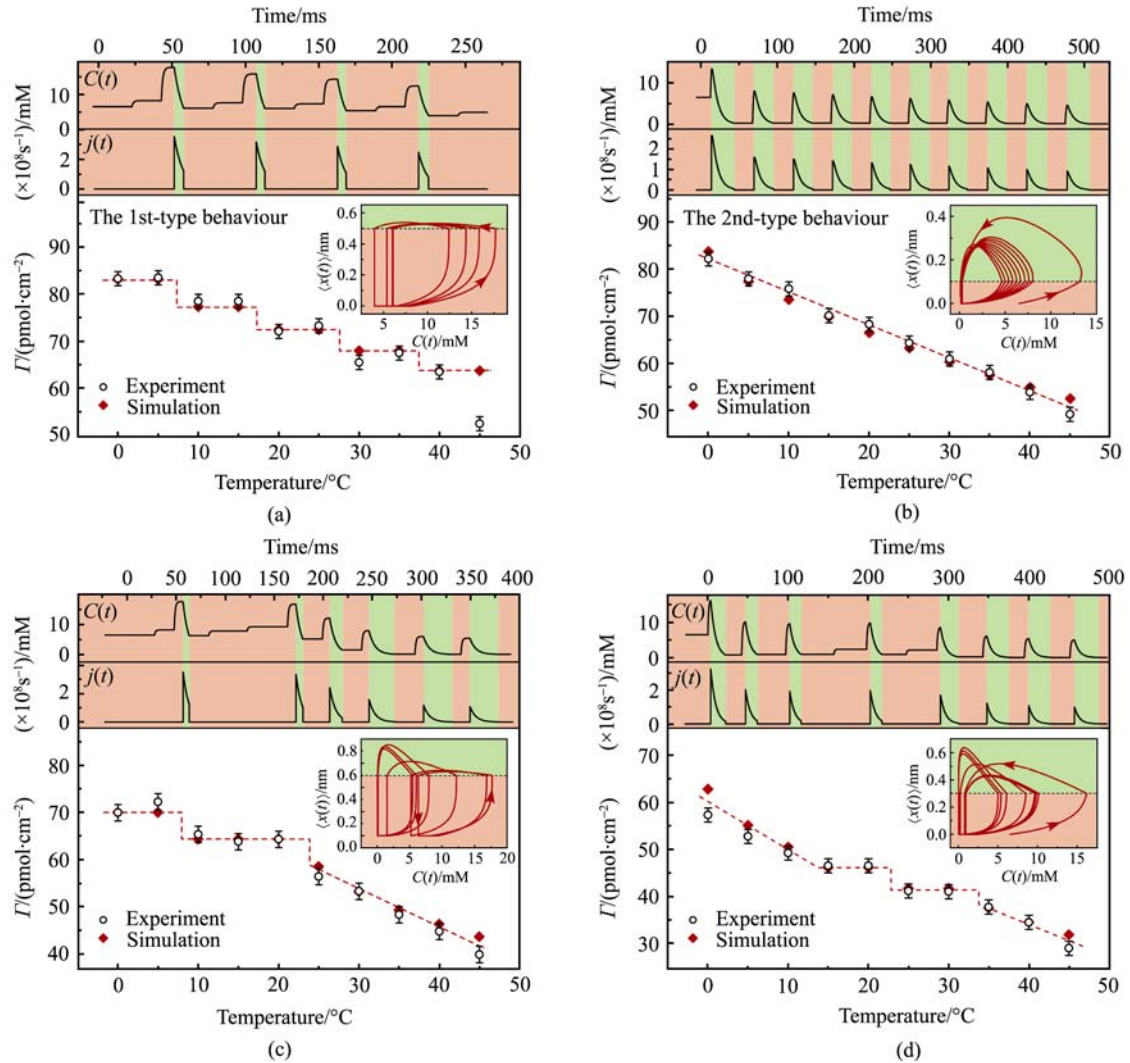


Fig. 10 (a) The first-type behaviour of I - T profile in the case of $C^* > C_{\max}$. (b) The first type behaviour of I - T profile in the case of $C^* < C_{\max}$. (c) The mixed behaviour in the case of one crossover between curves of C^* and C_{\max} at $T = T^*$ (≈ 25 °C). (d) The mixed behaviour in the case of two crossovers between curves of C^* and C_{\max} at $T = T_1^*$ (≈ 13 °C) and $T = T_2^*$ (≈ 33 °C). All experiments shown here are obtained with $T_c = 0$ °C. In each figure, the upper, middle, and bottom panels show, respectively, the computed temporal evolution of $C(t)$, $j(t)$, and the comparison between simulated I - T profile (filled square) and experimentally measured I - T profile (empty circle); the inset shows the mean trajectory of channel's reaction coordinate, with the first cycle marked by arrows; light red and light green mark the closed and open states of the channels respectively.

In this case, the DNA channels can be opened in every measurement step, leading to a linear decrease of I - T profiles [Fig. 10(b)].

Besides the two types, it is possible to observe both the stepwise and linear-decrease effects in the same I - T profiles, which arises from the crossovers of C^* and C_{\max} in the temperature range of interest. Figure 10 (c) demonstrates that a crossover of $C^* = C_{\max}$ taking place at $T = T^*$ (red line of Fig. 9) result in the first-type behavior at $T < T^*$ and the second-type behavior at $T > T^*$. Similar result with reverse sequence of the two behaviors is also observed, corresponding to the case of $C^* > C_{\max}$ at $T < T^*$ (dashed red line in Fig. 9). Fur-

thermore, two crossovers of C^* and C_{\max} (orange line in Fig. 9) give rise to a stepwise behavior sandwiched within the linear-decrease behavior in the I - T profile [Fig. 10(d)]. All possible kinds of I - T profiles predicted by our modeling quantitatively agree with experimental observations. This strongly validates our analyses of DNA channel gating.

The mechanism of DNA channel's gating is remarkably distinct from the gating mechanisms of protein channels. First, unlike the bistability nature of protein channels gating, in which both the open and closed conformations are among different local stable states [49, 50], the DNA channels show no bistability. A free DNA channel in equilibrium corre-

sponds to the minimum energy, which represents a stable closed state [Fig. 8(a)]. Only when the DNA channel dilates under the stress from the TH to reach the critical radius, the channel is permeable to TH. The open state of DNA channels is actually far away from equilibrium, showing a highly active trend to closing. Second, as the protein channels are formed by rigid binding (short-range interaction) between subunits, they are usually gated by membrane voltage or membrane tension rather than transport flux [49–51,60–64]. Our finding suggests that the DNA channels are gated by the channel-particle interactions due to their high flexibility. The calculations shown in Figs. 8 and 10 demonstrate that spatiotemporal coupling of DNA channel's gating with solute flux involves spontaneous periodic changes of the channel-particle interaction force $F(t)$ at nonequilibrium states, which gives rise to periodic oscillation of $C(t)$, $j(t)$ and $R(t)$, indicating a ratchet-like mechanism [65] for both channel's gating and solute permeation.

4 Conclusion

This study demonstrates reversible control of switching for DNA nanocompartment on surfaces. We show that a generality of DNA nanocompartment and its core property is invariant relative to the changes of specific substrate, selected indicator, and hybridization protocols. It is reasonable that its unique functions come from its dynamic nanostructure. While other researchers demonstrated surface switching for a low-density monolayer in wetting behavior [10], this study exhibits an alternative approach to reversibly switching surfaces with respect to molecular mechanical behavior, which shows possible applications in electrochemical energy storage, thermal molecule sensing, drug release, and nucleic acid analysis. Our results suggest that DNA nanocompartments could be used as building blocks for complex nanosystems, and that it promises to be integrated with the microfabrication and microfluidic technology to enable future biomaterial research [66].

In theoretical studies, we have established a simple coarse-grained model to simulate the melting transition of DNA in ADNC. The result provides a reasonable explanation for our experimental observations. Although the simulation method discretizes the Morse potential and stacking energy proposed in Peyrard-Bishop model, the result still present a comparable approximation to experimental data due to our fine treatment of energy changes during melting transition. We also established a stochastic model to modelize the dynamics of opening and closing of the ADNC. The results our simulation show a quantitative agreement

with the experimental observations. This gives a good confidence in describing the physical picture of the system, which will provides a theoretical guideline in the future studies along this line of research.

Acknowledgements The authors thank W. Deng, G. Y. Jin, X. M. Yu, Z. H. Zhang, R. S. Chen, D. P. Yu, S. Chang, S. X. Yang, and L. Jiang for different input in the research. This work was supported by the National Natural Science Foundation of China and Ministry of Science and Technology of China.

References

1. C. Mao, W. Sun, Z. Shen, and N. C. Seeman, *Nature*, 1999, 397: 144
2. B. Yuke, A. J. Turberfield, A. P. Jr Mills, F. C. Simmel, and J. L. Neumann, *Nature*, 2000, 406: 605
3. H. Yan, X. Zhang, Z. Shen, and N. C. Seeman, *Nature*, 2002, 415: 62
4. E. Braun, Y. Eichen, U. Sivan, and G. Ben-Yoseph, *Nature*, 1998, 391: 776
5. A. Y. Kasumov, et al., *Science*, 2001, 291: 280.
6. Y. Benenson, et al., *Nature*, 2001, 414: 430
7. E. Winfree, F. Liu, L. A. Wenzler, and N. C. Seeman, *Nature*, 1998, 394: 539
8. S. J. Park, A. Taton, and C. A. Mirkin, *Science*, 2002, 295: 1503
9. D. I. Gittins, D. Bethell, D. J. Schiffrin, and R. J. Nichols, *Nature*, 2000, 408: 67
10. J. Lahann, et al., *Science*, 2003, 299 : 371
11. Y. Mao, C. Luo, and Q. Ouyang, *Nucleic Acids Res.*, 2003, 31: e108
12. Y. Mao, et al., *Nucleic Acids Res.*, 2004, 32: e144
13. C. X. Luo, Y. D. Mao, and Q. Ouyang, *Acta Biophysica Sinica*, 2005, 21: 151
14. A. B. Steel, T. M. Herne, and M. J. Tarlov, *Anal. Chem.*, 1998, 70: 4670
15. T. M. Herne and M. J. Tarlov, *J. Am. Chem. Soc.*, 1997, 119: 8916
16. S. O. Kelley, et al., *Langmuir*, 1998, 14 : 6781
17. S. O. Kelley and K. B. Barton, *Bioconjugate Chem.*, 1997, 8: 31
18. Y. Okahata, et al., *Anal. Chem.*, 1998, 70: 1288
19. M. Yang, H. C. M. Yau, and H. L. Chan, *Langmuir*, 1998, 14: 6121
20. S. Chang, Y. D. Mao, and Q. Ouyang, *Journal of Physics: Conference Series*, 2006, 29: 18
21. Y. D. Mao, S. Chang, S. X. Yang, Q. Ouyang, and L. Jiang, *Nature Nanotechnology*, 2007, 2: 66
22. Z. Guo, R. A. Guilfoyle, A. J. Thiel, R. Wang, and L. M. Smith, *Nucleic Acids Res.*, 1994, 22: 5456
23. V. Paraschiv, et al., *Adv. Mater.*, 2002, 14: 722
24. T.W. Jing, et al., *Proc. Natl. Acad. Sci. USA*, 1993, 90: 8934
25. J. F. Allemand, D. Bensimon, R. Lavery, and V. Croquette, *Proc. Natl. Acad. Sci. USA*, 1998, 95: 14152
26. A. J. Bard and L. R. Faulkner, *Electrochemical methods*, New York: Wiley, 1980
27. E. Tuite and B. Nordén, *J. Am. Chem. Soc.*, 1994, 116: 7548
28. R. Rohs, H. Sklenar, R. Lavery, and B. Roder, *J. Am. Chem. Soc.*,

- 2000 122: 2860
29. C. Ohuigin, et al., *Nucleic Acids Res.*, 1987, 15: 7411
30. H. Aoki, P. Buhlmann, and Y. Umezawa, *Electroanalysis*, 2000, 12: 1272
31. M. T. Cater, M. Rodriguez, and A. J. Bard, *J. Am. Chem. Soc.*, 1989 111: 8901
32. D. H. Johnston and H. H. Thorp, *J. Phys. Chem.*, 1996, 100: 13837
33. G. D. Reid, et al., *J. Am. Chem. Soc.*, 2001, 123: 6953
34. S. Lifson, *J. Chem. Phys.*, 1964, 40: 3705
35. D. Poland and H. A. Scheraga, *J. Chem. Phys.*, 1966, 45: 1456
36. D. Poland and H. A. Scheraga, *J. Chem. Phys.*, 1966, 45: 1464
37. Y. L. Zhang, W. M. Zheng, J. X. Liu, and Y. Z. Chen, *Phys. Rev. E*, 1997, 56: 7100
38. N. Theodorakopoulos, T. Dauxois, and M. Peyard, *Phys. Rev. Lett.*, 2000, 85: 6
39. T. Dauxois and M. Peyard, *Phys. Rev. E*, 1995, 51: 4027
40. T. Dauxois and M. Peyard, *Phys. Rev. E*, 1993, 47: R44
41. B. H. Zimm and J. K. Bragg, *J. Chem. Phys.*, 1959, 28: 1246
42. H. M. Harreis, A. A. Kornyshev, C. N. Likos, H. Lowen, and G. Sutmann, *Phys. Rev. Lett.*, 2002, 89: 018303
43. H. M. Harreis, C. N. Likos, and H. Lowen, *Biophys. J.*, 2003, 84: 3607
44. A. A. Kornyshev and S. Leikin, *J. Chem. Phys.*, 1997, 107: 3656
45. A. A. Kornyshev, *Phys. Rev. E*, 2000, 62: 2576.
46. E. Allahyarov and H. Lowen, *Phys. Rev. E*, 2000, 62: 5542
47. A. A. Kornyshev, *Phys. Rev. Lett.*, 2001, 86: 3666
48. T. L. Hill, *J. Chem. Phys.*, 1959, 30: 383
49. I. Goychuk and P. Hänggi, *Proc. Natl. Acad. Sci. USA*, 2002, 99: 3552
50. P. Wiggins and R. Phillips, *Proc. Natl. Acad. Sci. USA*, 2004, 101: 4071
51. S. Markin and F. Sachs, *Phys. Biol.*, 2004, 1: 110
52. A. G. Cherstvy, A. A. Kornyshev, and S. Leikin, *J. Phys. Chem. B*, 2004, 108: 6508
53. A. A. Kornyshev and S. Leikin, *Phys. Rev. Lett.*, 2001, 86: 3666
54. P. A. Wiggins, et al., *Nature Nanotechnology*, 2006, 1: 137
55. T. Chou, *Phys. Rev. Lett.*, 1998, 80: 85
56. K. Hahn, J. Kärger, and V. Kukla, *Phys. Rev. Lett.*, 1996 76: 2762
57. R. S. Eisenberg, M. M. Klosek, and Z. Schuss, *J. Chem. Phys.*, 1995, 102: 1767
58. B. Nadler, Z. Schuss, and A. Singer, *Phys. Rev. Lett.*, 2005, 94: 218101
59. I. Kosztin and K. Schulten, *Phys. Rev. Lett.*, 2004, 93: 238102
60. B. Hille, *Ion Channels of Excitable Membranes*, Sunderland: Sinauer Associates, 2001
61. P. G. Gillespie and R. G. Walker, *Nature*, 2001, 413: 194
62. G. Yellen, *Nature*, 2002, 419: 35
63. R. MacKinnon, Nobel lecture, *Angew. Chem. Int. Ed.*, 2004, 43: 4265
64. E. Perozo, D. M. Cortes, P. Somporpisut, A. Kloda, and B. Marti-nac, *Nature*, 2002, 418: 942
65. M. Chinappi, E. De Angeles, S. Melchionna, C. M. Casciola, S. Succi, and R. Piva, *Phys. Rev. Lett.*, 2006, 97: 144509
66. J. Cheng and L. J. Kricka, *Biochip Technology*, Philadelphia PA: Harwood Academic Publishers, 2001